



Unveiling microstructural origins of the balanced strength–ductility combination in eutectic high-entropy alloys at cryogenic temperatures

Yi Li, Peijian Shi, Mingyang Wang, Yinpan Yang, Yan Wang, Yiqi Li, Yuebo Wen, Weili Ren, Na Min, Yan Chen, Yifeng Guo, Zhe Shen, Tianxiang Zheng, Ningning Liang, Wenjun Lu, Peter K. Liaw, Yunbo Zhong & Yuntian Zhu

To cite this article: Yi Li, Peijian Shi, Mingyang Wang, Yinpan Yang, Yan Wang, Yiqi Li, Yuebo Wen, Weili Ren, Na Min, Yan Chen, Yifeng Guo, Zhe Shen, Tianxiang Zheng, Ningning Liang, Wenjun Lu, Peter K. Liaw, Yunbo Zhong & Yuntian Zhu (2022) Unveiling microstructural origins of the balanced strength–ductility combination in eutectic high-entropy alloys at cryogenic temperatures, *Materials Research Letters*, 10:9, 602–610, DOI: [10.1080/21663831.2022.2078169](https://doi.org/10.1080/21663831.2022.2078169)

To link to this article: <https://doi.org/10.1080/21663831.2022.2078169>



© 2022 The Author(s). Published by Informa UK Limited, trading as Taylor & Francis Group



[View supplementary material](#)



Published online: 25 May 2022.



[Submit your article to this journal](#)



Article views: 1247



[View related articles](#)



[View Crossmark data](#)

Unveiling microstructural origins of the balanced strength–ductility combination in eutectic high-entropy alloys at cryogenic temperatures

Yi Li^{a*}, Peijian Shi^{a,b*}, Mingyang Wang^a, Yinpan Yang^a, Yan Wang^a, Yiqi Li^a, Yuebo Wen^a, Weili Ren^a, Na Min^{b,c}, Yan Chen^d, Yifeng Guo^a, Zhe Shen^a, Tianxiang Zheng^a, Ningning Liang^e, Wenjun Lu^f, Peter K. Liaw^g, Yunbo Zhong^a and Yuntian Zhu^b

^aState Key Laboratory of Advanced Special Steel & Shanghai Key Laboratory of Advanced Ferrometallurgy & School of Materials Science and Engineering, Shanghai University, Shanghai, People's Republic of China; ^bDepartment of Materials Science and Engineering, Hong Kong Institute for Advanced Study, College of Science and Engineering, City University of Hong Kong, Hong Kong, People's Republic of China; ^cLaboratory for Microstructures, Shanghai University, Shanghai, People's Republic of China; ^dCarl Zeiss (Shanghai) Co., Ltd, Shanghai, People's Republic of China; ^eSchool of Materials Science and Engineering, Nanjing University of Science and Technology, Jiangsu, People's Republic of China; ^fDepartment of Mechanical and Energy Engineering, Southern University of Science and Technology, Shenzhen, People's Republic of China; ^gDepartment of Materials Science and Engineering, The University of Tennessee, Knoxville, TN, USA

ABSTRACT

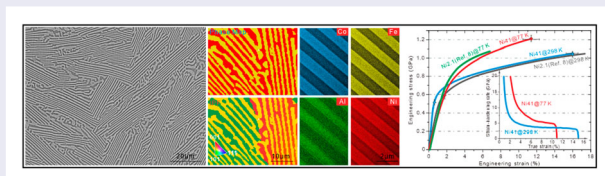
Eutectic high-entropy alloys (EHEAs) feature attractive strength–ductility balance at both ambient and cryogenic temperatures. Nevertheless, microstructural origins underpinning these balanced mechanical properties remain elusive. Here the deformation mechanisms of a recently-reported Al₁₉Co₂₀Fe₂₀Ni₄₁ EHEA were comparatively investigated at 298 and 77 K, which revealed a high frequency and density of dislocation multi-slip scenario in the soft eutectic lamellae and the corresponding compatible co-deformation in the adjacent hard lamellae that collectively endowed strong hetero-deformation-induced (HDI) hardening and excellent forest-dislocation hardening. Therefore, better ductility and tensile strength, in comparison to the other widely-studied EHEA system, could be sustained even at liquid-nitrogen temperatures.

ARTICLE HISTORY

Received 15 December 2021

KEYWORDS

Eutectic high-entropy alloys; mechanical properties; multi-slip scenario; compatible co-deformation; HDI hardening



IMPACT STATEMENT

We identify a new eutectic HEA system with superior strength–ductility combination at liquid-nitrogen temperatures, and provide critical microstructural insights and mechanisms into its enhanced cryogenic properties.

1. Introduction

High-entropy alloys (HEAs), initially conceptualized by Yeh and Cantor et al., are of great interest currently in the material community due to their unique metallurgy philosophies as well as exceptional mechanical and functional attributes [1–8]. To simultaneously obtain excellent strength and ductility, Lu et al. in 2014

proposed a new approach for engineering HEAs by taking advantage of the traditional eutectic alloy concept [9]. The resulting alloy system is the well-known eutectic HEAs (EHEAs), characterized with a balanced strength–ductility combination as well as good liquidity and castability [9–11]. Moreover, it has been reported that up to now, EHEAs possess many more appealing

CONTACT Peijian Shi ✉ shipeijian11@gmail.com Department of Materials Science and Engineering, Hong Kong Institute for Advanced Study, College of Science and Engineering, City University of Hong Kong, Hong Kong, China; ✉ State Key Laboratory of Advanced Special Steel & Shanghai Key Laboratory of Advanced Ferrometallurgy & School of Materials Science and Engineering, Shanghai University, Shanghai 200444, People's Republic of China; Yifeng Guo ✉ yfguo@shu.edu.cn ✉ State Key Laboratory of Advanced Special Steel & Shanghai Key Laboratory of Advanced Ferrometallurgy & School of Materials Science and Engineering, Shanghai University, Shanghai 200444, People's Republic of China; Yunbo Zhong ✉ yunboz@staff.shu.edu.cn ✉ State Key Laboratory of Advanced Special Steel & Shanghai Key Laboratory of Advanced Ferrometallurgy & School of Materials Science and Engineering, Shanghai University, Shanghai 200444, People's Republic of China

*These authors contributed equally to this work.

Supplemental data for this article can be accessed here. <https://doi.org/10.1080/21663831.2022.2078169>

© 2022 The Author(s). Published by Informa UK Limited, trading as Taylor & Francis Group

This is an Open Access article distributed under the terms of the Creative Commons Attribution License (<http://creativecommons.org/licenses/by/4.0/>), which permits unrestricted use, distribution, and reproduction in any medium, provided the original work is properly cited.

features, such as low phase-boundary energy, weak notch sensitivity, high thermal stability, attractive fatigue properties and so on [12–16]. The balanced mechanical properties of EHEAs sustained at the ultra-low temperature (77 K) have attracted extensive attention, which are highly demanded and critical for cryogenic-engineering applications [10,17].

Lu et al. [10] reported in the $\text{AlCoCrFeNi}_{2.1}$ EHEA that lowering tensile temperatures resulted in a continuous increase in yield strength, but the trade-off ductility did not decrease sharply, in which a decent strength–ductility combination was maintained even at 77 K. They explained that with decreasing temperature, dislocation motions become more difficult because of the reduced thermal energy for crossing Peierls-Nabarro barriers. Thus, more dislocations accumulate inside the crystal before moving out to accommodate the plastic strain, resulting in higher yield strength and less ductility. Moreover, they found that this trend is more severe in the ordered body-centered-cubic (B2) eutectic phase than in the adjacent ordered face-centred-cubic ($L1_2$) phase due to much higher temperature sensitivity of the Peierls-Nabarro force in the former.

However, the effect of low temperatures on tensile properties is investigated only in an $\text{AlCoCrFeNi}_{2.1}$ EHEA currently. It is unknown whether the excellent strength–ductility balance at 77 K is also accessible to other EHEA systems. Systematic characterization and comparative analysis of deformation behaviors at both room and cryogenic temperatures have been lacking, especially for the strain-partitioning EHEAs. Furthermore, to develop high-performance EHEAs that are more resistant to low temperatures, the corresponding deformation mechanisms of these EHEAs also deserve particularly comparative investigations.

2. Materials and methods

Two EHEAs, the recently-reported $\text{Al}_{19}\text{Co}_{20}\text{Fe}_{20}\text{Ni}_{41}$ and the widely-studied $\text{AlCoCrFeNi}_{2.1}$ (atomic percent, at%), were fabricated by arc-melting elemental ingredients with a purity > 99.95 (weight percent, wt%). To ensure uniformity, each alloy ingot (270 g in weight) was re-melted at least five times in a Ti-gettered high-purity argon atmosphere. The final composition uniformity was determined by scanning electron microscope (SEM) equipped with energy disperse spectroscopy (EDS), see Figure S1. Flat tensile specimens with a gauge size of 3.2 mm width, 1.2 mm thickness and 12.5 mm length were cut from two alloy ingots using electrical discharging, respectively. Tensile tests in air were conducted in an MTS testing machine with a constant strain rate of

$\sim 1 \times 10^{-3} \text{ s}^{-1}$ at 77 and 298 K. Each tensile specimen was repeated three times to ensure data reproducibility. SEM and electron back-scattering diffraction (EBSD) observations were performed on CamScan Apollo 300 SEM equipped with a HKL-Technology EBSD system. Transmission-electron microscopy (TEM), scanning TEM (STEM) and high-angle annular dark-field STEM (HAADF-STEM) were operated on JEOL-2100F and JEM-F200 at 200–300 kV. Samples for EBSD and TEM analysis were prepared by twin-jet electro-polishing, using 10% HClO_4 and 90% ethanol solution under -30°C .

3. Results and discussions

Herein, we selected the recently-reported $\text{Al}_{19}\text{Co}_{20}\text{Fe}_{20}\text{Ni}_{41}$ EHEA as a prototype material [18]. As observed in the widely-studied $\text{AlCoCrFeNi}_{2.1}$ EHEA [10,15,19,20], the backscattered electron (BSE) SEM image in Figure 1(a) reveals that the $\text{Al}_{19}\text{Co}_{20}\text{Fe}_{20}\text{Ni}_{41}$ EHEA has a typical as-cast eutectic lamellar microstructure. A statistically-distributed lamellar arrangement in the differently-oriented grains can be further identified by EBSD phase map and inverse pole figure (IPF) in Figure 1(b). In other words, the adjacent grains in the investigated EHEA exhibit different lamellar growth directions (Figure 1(a and b)). Moreover, the EBSD phase map (Figure 1(b)) reveals that the alternating coarse and fine lamellae in Figure 1(a) are FCC (face-centered-cubic) and BCC (body-centered-cubic) phases, respectively. These microstructural characteristics show great similarity to those of the widely-reported $\text{AlCoCrFeNi}_{2.1}$ EHEA [10,15,19,20]. However, the present $\text{Al}_{19}\text{Co}_{20}\text{Fe}_{20}\text{Ni}_{41}$ EHEA (Figure 1(a–c)) contains a higher content of the hard low-plasticity B2 phase (~ 45 vol.%) than that of the $\text{AlCoCrFeNi}_{2.1}$ EHEA (29–35 vol.%) [10,11,15,19,20].

To further understand the eutectic lamellar structure, we conducted multiple TEM analysis. A HAADF-STEM micrograph in Figure 1(c) reveals these alternating dual-phase eutectic lamellae with an average lamellae thickness of $\sim 1.65 \mu\text{m}$, which is very close to the measured result ($\sim 1.64 \mu\text{m}$) by EBSD and SEM. The accompanied selected-area electron diffraction (SAED) patterns (Figure 1(d)) suggest that the coarse (light) lamellae of $\sim 0.92 \mu\text{m}$ and the fine (gray) one of $\sim 0.73 \mu\text{m}$ in Figure 1(a–c) are ordered FCC ($L1_2$) and BCC (B2) phases, respectively. The ordering feature manifests itself with these weak superlattice spots, marked by the blue and red circles in two SAED images (Figure 1(d)). Further HAADF EDS maps in Figure 1(c) indicate that the B2 phase is depleted in Co and Fe but enriched in Al, and the adjacent $L1_2$ phase is only depleted in Al. Due

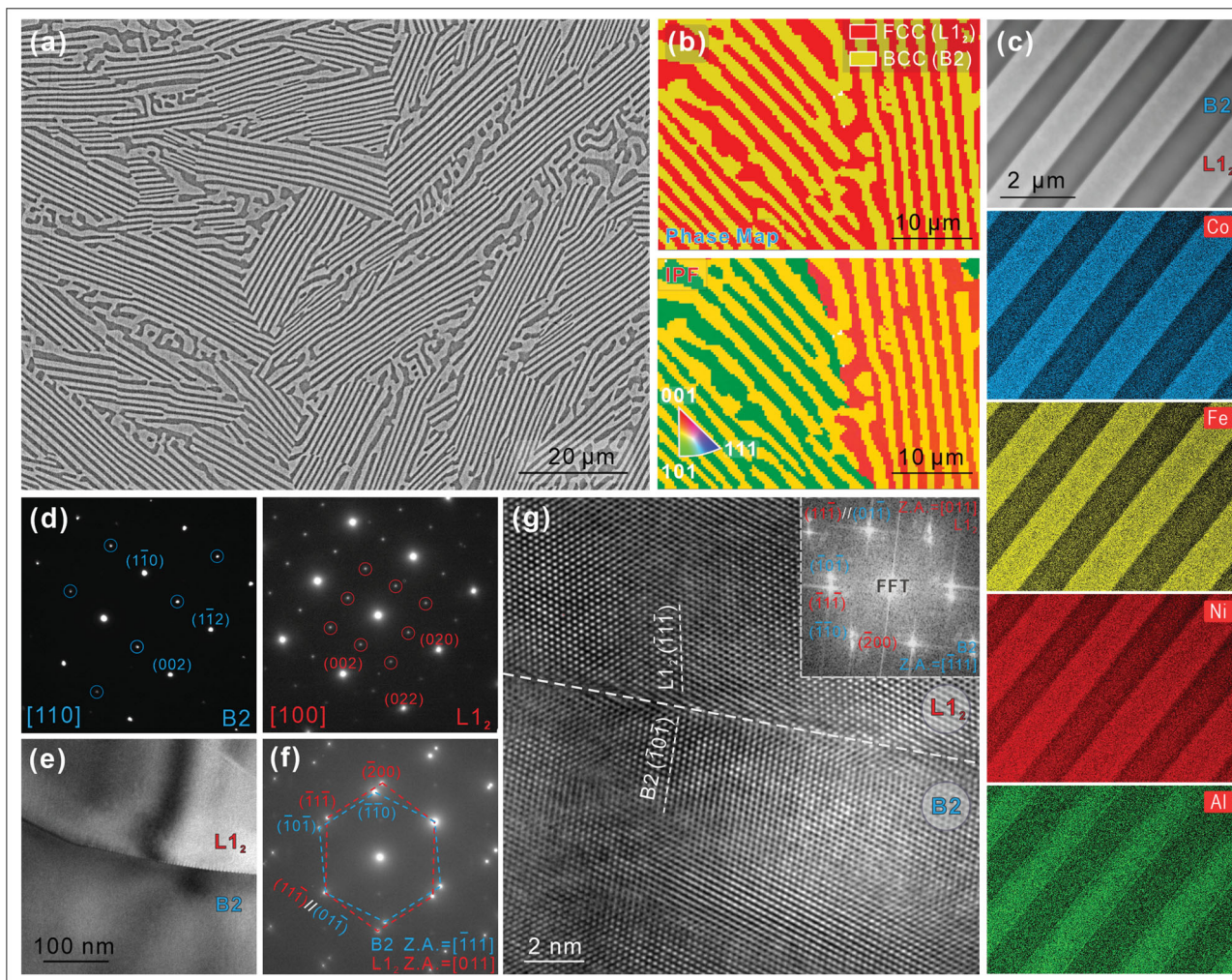


Figure 1. Typical eutectic lamellar microstructure of the as-cast $\text{Al}_{19}\text{Co}_{20}\text{Fe}_{20}\text{Ni}_{41}$ EHEA. (a) BSE-SEM image. (b) EBSD phase map (upper) and IPF (under). (c) HAADF-STEM image and EDS maps. (d) Two SAED patterns of B2 and L_{12} phases with superlattice diffraction spots marked by circles. (e, f) Enlarged TEM image of B2 and L_{12} phases and the corresponding SADP pattern. (g) HR-TEM image of B2 and L_{12} phases. The phase interface is marked by a white dotted line. The inset shows the corresponding FFT pattern, which helps get two lattice planes marked in each phase.

to higher Ni content in the $\text{Al}_{19}\text{Co}_{20}\text{Fe}_{20}\text{Ni}_{41}$ EHEA, the Ni element in the L_{12} and B2 two phases exhibits a relatively uniform distribution in comparison to the other three elements. This distribution trend was also observed in the $\text{AlCoCrFeNi}_{2.1}$ EHEA with high Ni content [21]. Figure 1(f) shows another SAED pattern collected from both L_{12} and B2 phases (Figure 1(e)), revealing that there exists a classical Kurdjumov-Sachs (K-S) orientation relationship between two phases [16]. Figure 1(g) displays further high-resolution TEM (HR-TEM) image of the inter-phase interface between these two phases. The interface is rough at the atomic scale, and in particular, exhibits a semi-coherent trait (Figure S2), which support a high interface-bonding strength [16]. Recently, the same K-S relationship and interface combination were also identified by Xiong et al. in the widely-studied $\text{AlCoCrFeNi}_{2.1}$ EHEA [13].

Note that although it has been well documented that in $\text{AlCoCrFeNi}_{2.1}$ EHEAs, there are dense Cr-rich nanoprecipitates with a disordered BCC-phase structure in these ordered B2-matrix lamellae of the present EHEA (Figure 1(a and b)). It is also confirmed by HAADF-STEM, EDS, TEM and HR-TEM multiscale characterizations (Figure 1(c, e and g)) that reveal much clean dual-phase eutectic lamellae. Our previous study reported that this difference might be attributed to the removal of the Cr element in the present EHEA $\text{Al}_{19}\text{Co}_{20}\text{Fe}_{20}\text{Ni}_{41}$, since the Cr element features a limited solid solubility usually in the NiAl-rich B2 phase [11,22,24,25]. So spherical nanoparticles often were detected in not only $\text{AlCoCrFeNi}_{2.1}$ EHEAs but also NiAl–Cr(Mo)-based alloys as well as these $\text{Al}_{0.8}\text{CrFeNi}_{2.2}$ and AlCrFeNi_3 EHEAs [11,22,24,25].

Table 1. Similarities and differences between these two AlCoCrFeNi_{2.1} (termed as Ni_{2.1}) and Al₁₉Co₂₀Fe₂₀Ni₄₁ (Ni₄₁) EHEAs [9–11,13,20,21].

	Phase	Lamellar thickness (μm)	Phase content (vol%)	Hardness (GPa)	Grain size (μm)	Interface feature	Interplanar spacing (Å)
Ni _{2.1}	L1 ₂	~ 1.15	65 ~ 71	4.0 ~ 6.0	43	K-S	d ₍₁₁₁₎ = 2.06
	B2	~ 0.81	29 ~ 35	7.5 ~ 12.0			d ₍₁₁₀₎ = 2.08
Ni ₄₁	L1 ₂	~ 0.92	~ 55	~ 4.2	35	K-S	d ₍₁₁₁₎ = 2.06
	B2	~ 0.73	~ 45	~ 5.6			d ₍₁₁₀₎ = 2.03

On the basis of the above microstructure analysis and comparison, Table 1 outlines the similarities and differences between these two EHEAs of AlCoCrFeNi_{2.1} and Al₁₉Co₂₀Fe₂₀Ni₄₁. Figure 2 exhibits the corresponding tensile behaviors of these two EHEA specimens, at both room and cryogenic temperatures (298 and 77 K). At room temperature, the yield and tensile strengths of these two EHEAs are almost the same, which are ~ 540 MPa and ~ 1,050 MPa, respectively. The elongation to fracture is 16 ~ 18% in these two EHEAs. Compared to the room-temperature properties, both yield and tensile strengths in two EHEA specimens are elevated slightly (60 ± 15 MPa), which is in trade-off with elongation. Yet still, a quite good combination of strength and ductility is maintained at the cryogenic temperature of 77 K, especially in the as-investigated Al₁₉Co₂₀Fe₂₀Ni₄₁ EHEA. In view of the mechanical response previously captured in the AlCoCrFeNi_{2.1} EHEA [10], the current property trend further substantiates EHEAs featured with the excellent resistance of the ductile-to-brittle transition at ultralow temperatures. This behavior, therefore, sustained the balance of strength and ductility observed in Figure 2.

After identifying the balanced strength–ductility combination at the ultralow temperature (77 K), it naturally follows to analyze the deformation and strengthening mechanisms in the as-cast eutectic lamellar microstructure.

First, although these two EHEAs are composed of different phase contents (the major difference; Table 1), they have comparable yield strengths (Figure 2). This abnormal trend may stem from substantial hardness differences of the same phase, as previously identified in these two EHEAs [26–28]. Through multiple nano-indentation tests, for example, Shi et al. [26] reported the L1₂ and B2 phases with the hardness of ~ 4.2 GPa and ~ 5.6 GPa, respectively, in the Al₁₉Co₂₀Fe₂₀Ni₄₁, while Bhattacharjee and Muskeri et al. [27,28] showed the hardness ranges of 4.0 ~ 6.0 GPa and 7.5 ~ 12.0 GPa of the L1₂ and B2 phases, respectively, in the AlCoCrFeNi_{2.1}. These reported empirical relationships between hardness and yield strength usually suggest that a higher hardness can represent larger yield strength in metallic

materials [29]. Given their similar eutectic microstructures and comparable lamellar thicknesses (Table 1), it is expected that if these two EHEAs have the same B2-phase content, the AlCoCrFeNi_{2.1} EHEA should exhibit larger yield strength, due to its B2 eutectic phase with higher hardness in comparison to that of the Al₁₉Co₂₀Fe₂₀Ni₄₁. However, the Al₁₉Co₂₀Fe₂₀Ni₄₁ EHEA, in fact, contains a higher B2-phase content (~ 45 vol.%) than that of the AlCoCrFeNi_{2.1} EHEA (29 ~ 35 vol.%) [11,19]. Therefore, it could be deduced that the differences of phase content and hardness collectively enable the observed comparable yield strengths (Figure 2). Indeed, there are many factors contributing to this comparable property, and more factors are worthy of further study.

Second, as predicted by the Considère criterion [30], ductility is derived from the strain-hardening capability, in which high strain hardening can prevent mechanical instability (i.e. a localization of strain via necking) and thus render excellent ductility [26,31–33]. To identify the strain-hardening origin of the investigated Al₁₉Co₂₀Fe₂₀Ni₄₁ EHEA, we conducted careful microstructure characterizations at different strain levels, using (two-beam) TEM-imaging techniques (Figure 3).

At the low tensile strain of ~ 3%, a bright-field TEM (BF-TEM) image (Figure 3(a)) reveals that some defect arrays operate in the L1₂ lamellae, whereas no visible defects appear in the B2 lamellae. This deformation behavior, as discussed above, can be reasonably ascribed to the B2 phase with far higher hardness than that of the L1₂ phase. This case implies that a higher critical stress is required to activate plastic deformation of the hard B2 phase [16,26]. When the tensile strain is increased to ~ 6%, a BF-TEM image (Figure 3(b)) suggests that these defect arrays operating in the L1₂ lamellae become more active and intensive, characterized with a high density of parallel dislocations along the (11 $\bar{1}$) primary slip bands.

These parallel dislocations within slip bands, piled up against the phase interface, are known as geometrically necessary dislocations (GNDs) (Figure 3(b)) [20,26,31]. Concomitant with these peculiar dislocation configurations and operations, high back stress and hardening are expected in the L1₂ lamellae, especially around the phase interface [26]. Upon tensile deformation, this back stress

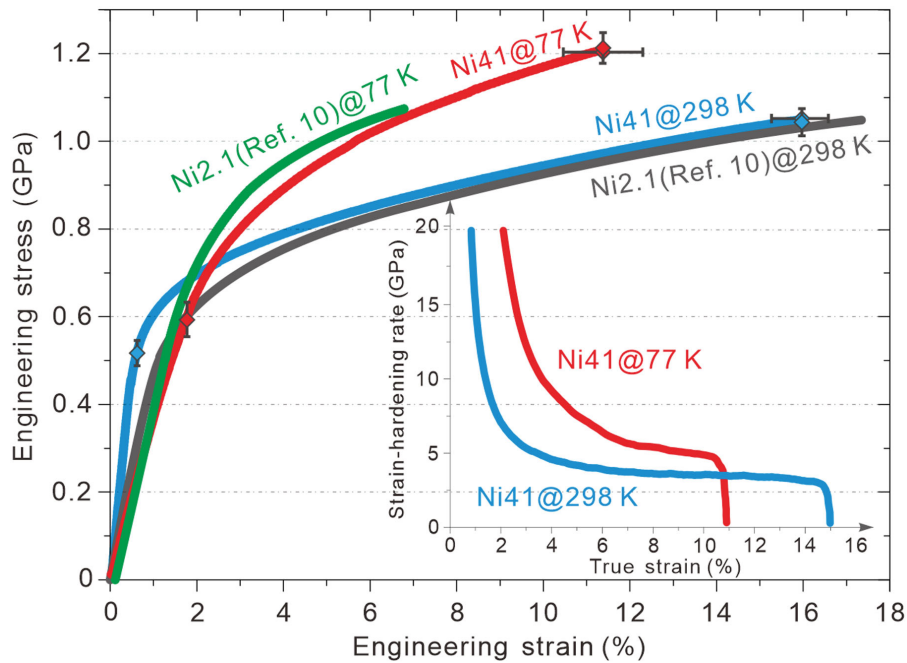


Figure 2. Tensile response of the as-investigated $\text{Al}_{19}\text{Co}_{20}\text{Fe}_{20}\text{Ni}_{41}$ EHEA (termed as Ni41) and the widely-reported $\text{AlCoCrFeNi}_{2.1}$ EHEA (Ni2.1; Ref. 10) at 77 and 298 K. The error bars are standard deviations of the mean. The inset shows the corresponding strain-hardening curves of the as-investigated $\text{Al}_{19}\text{Co}_{20}\text{Fe}_{20}\text{Ni}_{41}$ EHEA at 77 and 298 K.

can exert a forward stress on the adjacent hard B2 lamellae, activating its progressive plastic deformation [26,34]. As displayed by the dark-field TEM image in Figure 3(c), a few planar-slip dislocations gradually nucleate at the phase interface and slip towards the B2 lamellar interior at the medium strain of $\sim 6\%$. Moreover, these above dislocation behaviors are also well facilitated by these accepted general dislocation characteristics, in which edge dislocations are usually plentiful in the L_{12} phase, while screw dislocations in the B2 phase [8,35–37]. These dynamic dislocation activities promote compatible co-deformation of adjacent two phases in the as-cast eutectic lamellae structure, which can effectively avert stress concentrations and the attendant phase-interface debonding [26].

This compatible co-deformation is also detected by EBSD observations, in which the kernel average misorientation (KAM) values, indicative of the degree of plastic deformation, are obviously greater than zero in both phases. Moreover, a gradient distribution of KAM values can be observed in the L_{12} phase around the phase interface, which well matches the profuse GND piling-ups detected by TEM in Figure 3(a and b). The average KAM values of B2 and L_{12} phases are ~ 0.42 and ~ 0.71 , respectively, which quantitatively confirm the hetero-deformation scenario developed from strain partitioning among these soft and hard alternating phases (Figure 3(a–c)). Thus, an extra strain-hardening incident

can be achieved, i.e. the well-known hetero-deformation-induced (HDI) hardening [31,34]. This HDI hardening, as revealed by Zhu et al. [34], is kinematic, directional, and associated with extensive GND pile-up, which can enhance ductility.

Meanwhile, the observed GND configuration and its HDI hardening also corroborate and rationalize the reported high HDI stress [quantified by loading-unloading-reloading (LUR) experiments prevailing in EHEAs recently 20,26,31,38]. When further increasing the tensile strain ($\sim 12\%$), secondary (and even multiple) slip systems are gradually activated in the L_{12} lamellae (as revealed by Figure 3(d) and the enlarged Figure 3(e)). Therefore, the ever-increasing forest-dislocation hardening and HDI hardening are achieved, which prevent premature plastic instability and endow excellent ductility even at the ultralow liquid-nitrogen temperature (Figure 2) [26,34].

During the cryogenic tensile deformation, the corresponding SAED patterns did not exhibit the traits of twinning and/or phase transformation in both phase of the $\text{Al}_{19}\text{Co}_{20}\text{Fe}_{20}\text{Ni}_{41}$ EHEA (Figure 3(g and h)). But interestingly, the ordered spots and especially the principal spots in these SAEDs of L_{12} phase gradually diffuse and elongate as tensile strain increases (Figure 3(g)). The spot diffusion and elongation can be reasonably ascribed to these detected deformation incidents in Figure 3(a–d), i.e. the GND-induced strain gradient around the lamellar

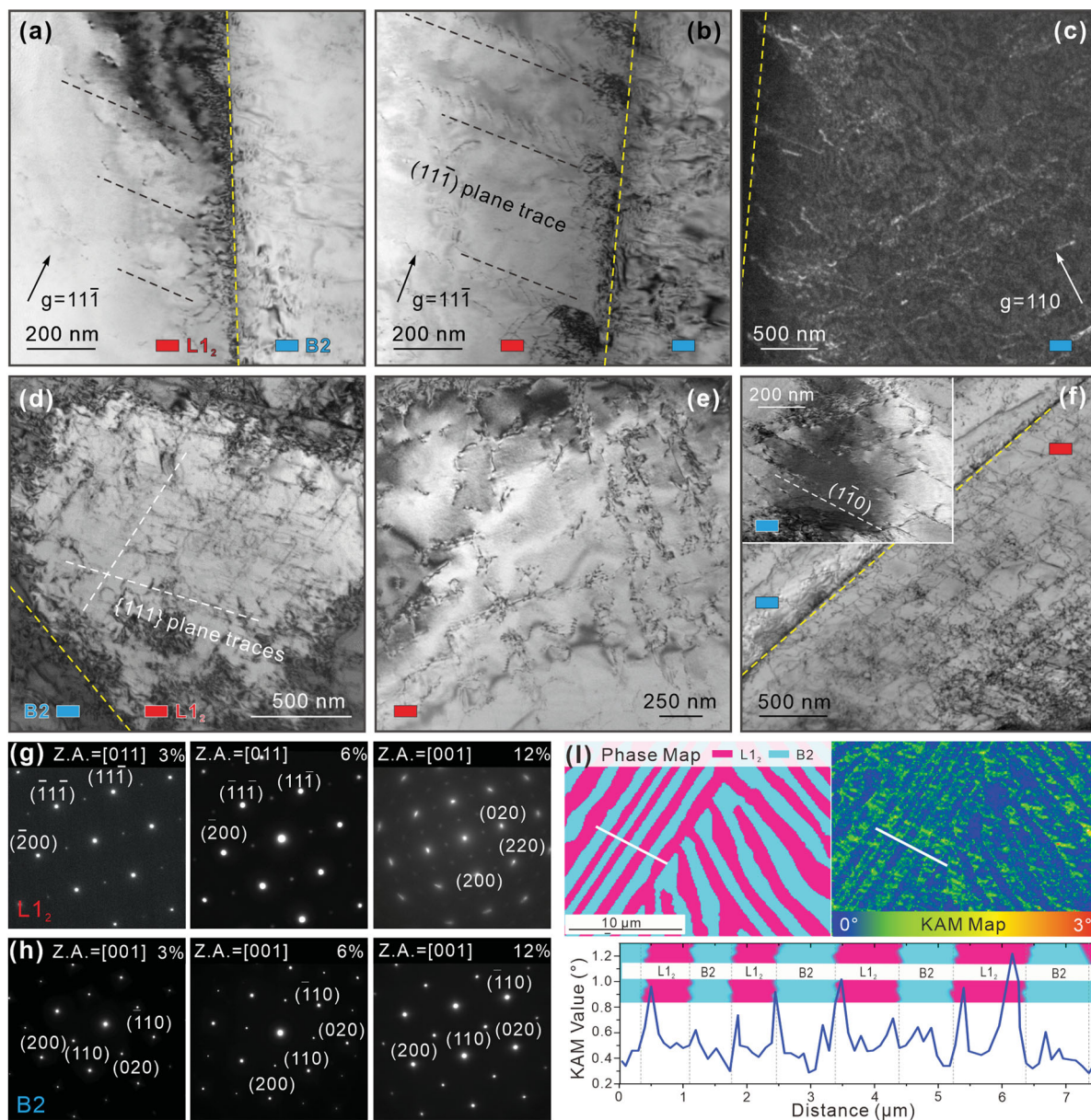


Figure 3. Typical TEM images showing deformation microstructures of the as-investigated $\text{Al}_{19}\text{Co}_{20}\text{Fe}_{20}\text{Ni}_{41}$ EHEA under different strain conditions: (a) $\sim 3\%$, (b, c) $\sim 6\%$ and (d, e) $\sim 12\%$ at 77 K; (f) $\sim 16\%$ at 298 K. g indicates the direction of the diffraction vector. All phase interfaces are marked by yellow dotted lines. (g and h) The corresponding SAEDs of L_{12} and B2 phase, respectively, at $\sim 3\%$, $\sim 6\%$ and $\sim 12\%$. (i) EBSD phase map, KAM map, and the corresponding curve of KAM values from these locations marked by white line in the KAM map.

interface as well as high frequency and density of dislocation multi-slips within the lamellar interior. The resulting dynamic substructure refinement can achieve the gradual increase of lamellar misorientation, characterized by these diffused and elongated spots [39,40].

Third, to further illuminate the excellent strain hardening and ductility at 77 K, we also investigated and compared the deformation mechanisms of the $\text{Al}_{19}\text{Co}_{20}\text{Fe}_{20}\text{Ni}_{41}$ EHEA at room temperature (298 K) as well as the $\text{AlCoCrFeNi}_{2.1}$ EHEA at the ultralow temperature (77 K).

After close microstructure characterizations, we found that in the $\text{Al}_{19}\text{Co}_{20}\text{Fe}_{20}\text{Ni}_{41}$ EHEA the room-temperature loading circumstance rendered a higher degree of defect activities (i.e. dislocation accumulation and interaction) than at 77 K. For example, in the post-fracture microstructure, a higher frequency and density of multi-slip scenario could be detected in the L_{12} lamellae at 298 K. This multi-slip scenario, revealed in Figure 3(f), manifests itself with nano-scale dislocation networks of planar dislocation arrays, and even sporadic dislocation cells due to dislocation cross-slips [16,26,32].

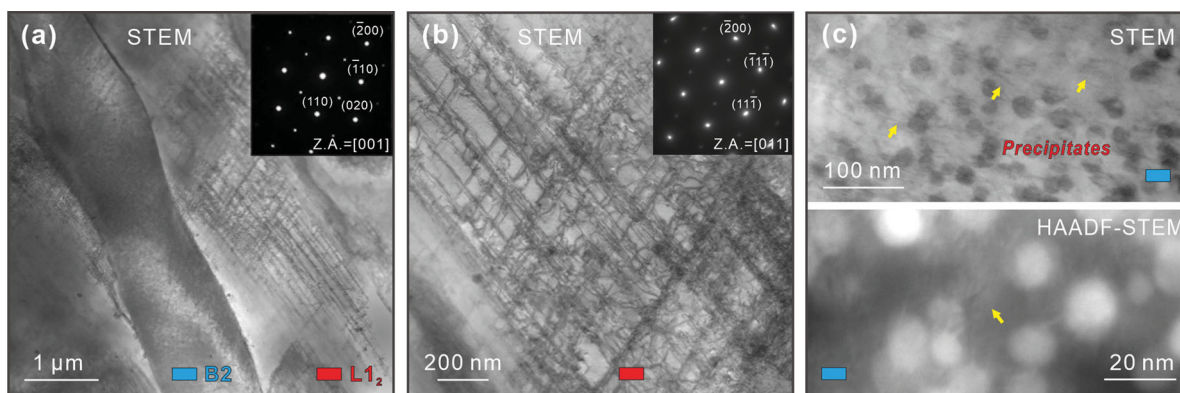


Figure 4. Deformation microstructures in the post-fracture AlCoCrFeNi_{2.1} EHEA at 77 K. (a, b) STEM image and the enlarged STEM image showing a multi-slip dislocation scenario in the L₁₂ phase. These two insets are the SAED patterns of B2 and L₁₂ phases, respectively. (c) Upper STEM image and under HAADF-STEM image exhibiting dense Cr-rich precipitates and a few dislocation debris in the B2 phase.

Concurrently, denser dislocation operations were also detected in the B2 lamellae, characterized with much smaller average dislocation spacing (~ 190 nm, as indicated by the inset of Figure 3(f)). Therefore, a higher dislocation density is potentially accompanied with stronger back-stress hardening and forest-dislocation hardening. Consequently, these trends, as quantified by the inset of Figure 2, support a longer lasting strain-hardening capacity, which produced the observed larger room-temperature tensile ductility (Figure 2).

Here the relatively-lower dislocation storage at 77 K is due to the fact that the ultralow deformation temperature weakens the intensity of thermal activation [10,41], making dislocation slip more difficult (that elevates the flow stress in Figure 2). Therefore, at the liquid-nitrogen temperature deformation twinning (DT) is readily triggered to assist in plastic deformation if the investigated materials have low stacking fault energies (SFEs) [31,41]. Moreover, in the L₁₂ phase of the current Al₁₉Co₂₀Fe₂₀Ni₄₁ EHEA, the DT propensity should be more preferred, since its dual-phase lamellar architecture readily develops high local back stress at the hetero-phase interfaces that can help stimulate DT upon stress loading [31,34]. However, we failed to detect the anticipated DT scenario in the post-fracture microstructure (insets of Figure 4(a and b)), indicating that the L₁₂ phase of Al₁₉Co₂₀Fe₂₀Ni₄₁ has relatively high SFE. Otherwise, an improved low-temperature ductility will be realized, as widely reported in these CoCrNi medium-entropy alloys and CoCrFeMnNi HEAs with low SFEs ($22 \sim 30$ mJ·m⁻²) [41–47]. Interestingly, due to the prevailing HDI hardening, the current Al₁₉Co₂₀Fe₂₀Ni₄₁ exhibits obviously higher cryogenic ductility and smaller ductility loss than the widely-studied AlCoCrFeNi_{2.1}.

Similarly, at the liquid-nitrogen temperature, we only observed lattice dislocations (without the DT incident) in

both phases of the AlCoCrFeNi_{2.1} EHEA (Figure 4(a–c)). This deformation behavior is analogous to those findings reported by Lu and Bhattacharjee et al. [10,17]. Specifically, we also identified a high density of multi-slip scenario in the L₁₂ lamellae of the AlCoCrFeNi_{2.1} alloy (Figure 4(b)). However, differentiating from that of the current Al₁₉Co₂₀Fe₂₀Ni₄₁, the adjacent B2 lamellae in the post-mortem AlCoCrFeNi_{2.1} only show a few dislocation debris (marked by yellow arrows in Figure 4(c)). In addition to the reduced thermal activation at 77 K, the B2 phase of the AlCoCrFeNi_{2.1} with substantial Cr-enriched precipitate strengthening (Figure 4(c)) might be more difficult to be plastically deformed than that of the Al₁₉Co₂₀Fe₂₀Ni₄₁ [10,11,20]. Hence, it is conceivable that the HDI hardening effect will not work as well as in the current Al₁₉Co₂₀Fe₂₀Ni₄₁ EHEA.

From the perspective of the phase constitution, one could speculate that in the AlCoCrFeNi_{2.1} EHEA the soft L₁₂ phase with abundant multi-slip dislocations endows some decent ductility at 77 K, while the adjacent B2 phase with far higher hardness features strong deformation resistance that equips high strength. Nevertheless, the limited plastic deformability of the B2 phase unfortunately leads to a compromised hardening capability (i.e. exhibiting lower ductility and tensile strength of the AlCoCrFeNi_{2.1} than that of the Al₁₉Co₂₀Fe₂₀Ni₄₁ in Figure 2) [16,20,26]. Moreover, the trench-like fracture morphology with great depth-shallow fluctuations (Figure S3) also suggests a poor plasticity of the B2 phase, which cannot support coordinated co-deformation of two adjacent phases and thus, triggers a premature fracture failure of the AlCoCrFeNi_{2.1} EHEA [11,26,34].

These above comparative analysis and results based on deformation microstructures of two as-cast EHEAs are also confirmed by the quantitative LUR mechanical tests (detailing in Figure S4). Here, as reported in

Ref. [48] and [49], we divided the flow stress into the back stress (also termed as HDI stress, recently) associated with a long-range stress on mobile dislocations and the effective stress required locally for the dislocation movement. In the early stage of deformation (< 8%), the extensive GND pile-ups in the $L1_2$ lamellae produce very high back stress, about twice the effective stress. With increasing tensile strains, the dislocation multi-slips and the plastic deformation in $L1_2$ and B2 phases, respectively, effectively elevate the effective stress in the $Al_{19}Co_{20}Fe_{20}Ni_{41}$ EHEA. But the back stress or HDI stress in both as-cast EHEAs still dominates the overall flow stress, and the resulting extra HDI hardening, concomitant with appreciable forest-dislocation hardening, contributes to excellent strain-hardening capability.

4. Conclusions

The present study demonstrates that a balanced (and even better) strength–ductility balance at 77 K is accessible to the other EHEA systems. Through multi-scale microstructure analysis, we explain the origin for the first time that these two $Al_{19}Co_{20}Fe_{20}Ni_{41}$ and $AlCoCrFeNi_{2.1}$ alloys have different phase contents but exhibit comparable mechanical properties at room temperature, and of special interest, corroborate the existence of plentiful GND pile-up around the phase interfaces that rationalizes the reported high HDI stress prevailing in EHEAs as well as the HDI property enhancement at cryogenic temperature. Specifically, in the $Al_{19}Co_{20}Fe_{20}Ni_{41}$ EHEA, these dynamic hetero-deformation scenarios developed from strain partitioning among soft and hard eutectic phases enable an extra HDI hardening incident, which, together with forest-dislocation hardening, promotes the simultaneous strength–ductility enhancement at 77 K. In the $AlCoCrFeNi_{2.1}$ counterpart, the poor plastic deformability of B2 phase serves as the ‘short slab’ that results in the observed inferior low-temperature properties. Over recent years, some unusual dislocation behaviors have been identified in HEAs with highly concentrated solid solutions, due to local concentration fluctuations or chemical short-range order (SRO), and even the deformation-induced transformation from long-range order to SRO at the atomic scale [42,50,51]. In a follow-up project, we will try to investigate the multiple interactions between lattice dislocations and element distribution, and advance our fundamental understanding of the intrinsic deformation behaviors of advanced EHEAs at low homologous temperatures.

Disclosure statement

No potential conflict of interest was reported by the author(s).

Funding

The work was financially supported by National Key Research and Development Program of China [grant numbers 2018YFF0109404, 2016YFB0300401, 2016YFB0301401]; National Natural Science Foundation of China [grant numbers U1732276, U1860202] and National Natural Science Foundation of China [grant number 52004156].

ORCID

Na Min  <http://orcid.org/0000-0001-6343-1244>

Yuntian Zhu  <http://orcid.org/0000-0002-5961-7422>

References

- [1] Yeh JW, Chen SK, Lin SJ, et al. Nanostructured high-entropy alloys with multiple principal elements: novel alloy design concepts and outcomes. *Adv Eng Mater.* 2004;6(5):299–303.
- [2] Cantor B, Chang ITH, Knight P, et al. Microstructural development in equiatomic multicomponent alloys. *Mater Sci Eng A.* 2004;375–377:213–218.
- [3] Zhang Y, Zuo TT, Tang Z, et al. Microstructures and properties of high-entropy alloys. *Prog Mater Sci.* 2014;61:1–93.
- [4] He MY, Shen YF, Jia N, et al. C and N doping in high-entropy alloys: A pathway to achieve desired strength-ductility synergy. *Appl Mater Today.* 2021;25:101162.
- [5] Gasan H, Lökçü E, Ozcan A, et al. Effects of Al on the phase volume fractions and wear properties in the $Al_xCoCrFeMoNi$ high entropy alloy system. *Met Mater Int.* 2020;26:310–320.
- [6] Wang CT, He Y, Guo ZP, et al. Strain rate effects on the mechanical properties of an $AlCoCrFeNi$ high-entropy alloy. *Met Mater Int.* 2021;27:2310–2318.
- [7] Ding ZY, He QF, Chung D, et al. Evading brittle fracture in submicron-sized high entropy intermetallics in dual-phase eutectic microstructure. *Scr Mater.* 2020;187:280–284.
- [8] George EP, Raabe D, Ritchie RO. High-entropy alloys. *Nat Rev Mater.* 2019;4:515–534.
- [9] Lu YP, Dong Y, Guo S, et al. A promising new class of high-temperature alloys: eutectic high-entropy alloys. *Sci Rep.* 2014;4:6200.
- [10] Lu YP, Gao XZ, Li J, et al. Directly cast bulk eutectic and near-eutectic high entropy alloys with balanced strength and ductility in a wide temperature range. *Acta Mater.* 2017;124:143–150.
- [11] Gao XZ, Lu YP, Zhang B, et al. Microstructural origins of high strength and high ductility in an $AlCoCrFeNi_{2.1}$ eutectic high-entropy alloy. *Acta Mater.* 2017;147:59–66.
- [12] Zhang W, Liu L, Peng SY, et al. The tensile property and notch sensitivity of $AlCoCrFeNi_{2.1}$ high entropy alloy with a novel “steel-frame” eutectic microstructure. *J Alloy Compd.* 2021;863:158747.
- [13] Xiong T, Yang WF, Zheng SJ, et al. Faceted Kurdjumov-Sachs interface-induced slip continuity in the eutectic high-entropy alloy, $AlCoCrFeNi_{2.1}$. *J Mater Sci Technol.* 2021;65:216–227.
- [14] Jiang H, Qiao DX, Lu YP, et al. Direct solidification of bulk ultrafine-microstructure eutectic high-entropy

- alloys with outstanding thermal stability. *Scr Mater.* **2019**;165:145–149.
- [15] Shukla S, Wang TH, Cotton S, et al. Hierarchical microstructure for improved fatigue properties in a eutectic high entropy alloy. *Scr Mater.* **2018**;156:105–109.
- [16] Shi PJ, Li Y, Wen YB, et al. A precipitate-free AlCoFeNi eutectic high-entropy alloy with strong strain hardening. *J Mater Sci Technol.* **2021**;89:88–96.
- [17] Bhattacharjee T, Zheng RX, Chong Y, et al. Effect of low temperature on tensile properties of AlCoCrFeNi_{2.1} eutectic high entropy alloy. *Mater Chem Phys.* **2018**;210:207–212.
- [18] Jin X, Zhou Y, Zhang L, et al. A novel Fe₂₀Co₂₀Ni₄₁Al₁₉ eutectic high entropy alloy with excellent tensile properties. *Mater Lett.* **2018**;216:144–146.
- [19] Wani IS, Bhattacharjee T, Sheikh S, et al. Ultrafine-grained AlCoCrFeNi_{2.1} eutectic high-entropy alloy. *Mater Res Lett.* **2016**;4:174–179.
- [20] Shi PJ, Ren WL, Zheng TX, et al. Enhanced strength-ductility synergy in ultrafine-grained eutectic high-entropy alloys by inheriting microstructural lamellae. *Nat Commun.* **2019**;10:489.
- [21] Wang QN, Lu YP, Yu Q, et al. The exceptional strong face-centered cubic phase and semi-coherent phase boundary in a eutectic dual-phase high entropy alloy AlCoCrFeNi. *Sci Rep.* **2018**;8:1–7.
- [22] Jin X, Bi J, Zhang L, et al. A new CrFeNi₂Al eutectic high entropy alloy system with excellent mechanical properties. *J Alloy Compd.* **2019**;770:655–661.
- [23] Xiong T, Zheng SJ, Pang JY, et al. High-strength and high-ductility AlCoCrFeNi_{2.1} eutectic high-entropy alloy achieved via precipitation strengthening in a heterogeneous structure. *Scr Mater.* **2020**;186:336–340.
- [24] Dong Y, Yao ZQ, Huang X, et al. Microstructure and mechanical properties of AlCo_xCrFeNi_{3-x} eutectic high-entropy-alloy system. *J Alloy Compd.* **2020**;823:153886.
- [25] Wang L, Shen J, Shang Z, et al. Microstructure evolution and enhancement of fracture toughness of NiAl–Cr(Mo)–(Hf,Dy) alloy with a small addition of Fe during heat treatment. *Scr Mater.* **2014**;89:1–4.
- [26] Shi PJ, Li RG, Li Y, et al. Hierarchical crack buffering triples ductility in eutectic herringbone high-entropy alloys. *Science.* **2021**;373:912–918.
- [27] Bhattacharjee T, Wani IS, Sheikh S, et al. Simultaneous strength-ductility enhancement of a nano-lamellar AlCoCrFeNi_{2.1} eutectic high entropy alloy by cryo-rolling and annealing. *Sci Rep.* **2018**;8:1–8.
- [28] Saideep M, Vahid H, Riyadh S, et al. Small-scale mechanical behavior of a eutectic high entropy alloy. *Sci Rep.* **2020**;10:2669.
- [29] Zhang P, Li SX, Zhang ZF. General relationship between strength and hardness. *Mater Sci Eng A.* **2011**;529:62–73.
- [30] Meyers M, Chawla KK. *Mechanical behavior of materials.* New York: Cambridge University Press; **2009**.
- [31] Shi PJ, Zhong YB, Li Y, et al. Multistage work hardening assisted by multi-type twinning in ultrafine-grained heterostructural eutectic high-entropy alloys. *Mater Today.* **2020**;41:62–71.
- [32] He ZF, Jia N, Yan HL, et al. Multi-heterostructure and mechanical properties of N-doped FeMnCoCr high entropy alloy. *Int J Plasticity.* **2021**;139:102965.
- [33] Jia YF, Jia YD, Wu SW, et al. Novel ultralight-weight complex concentrated alloys with high strength. *Materials (Basel).* **2019**;12:1136.
- [34] Zhu YT, Ameyama K, Anderon PM, et al. Heterostructured materials: superior properties from hetero-zone interaction. *Mater Res Lett.* **2021**;9:1–31.
- [35] Li ZZ, Zhao ST, Ritchie RO, et al. Mechanical properties of high-entropy alloys with emphasis on face-centered cubic alloys. *Prog Mater Sci.* **2019**;102:296–345.
- [36] Takasugi T, Hanada S, Izumi O. Slip modes in B2-type intermetallic alloys. *Mater Tran JIM.* **1990**;31(6):435–442.
- [37] Liu CT, George EP, Maziasz PJ, et al. Recent advances in B2 iron aluminide alloys: deformation, fracture and alloy design. *Mater Sci Eng A.* **1998**;258(1-2):84–98.
- [38] Zhu YC, Zhou SC, Xiong ZP, et al. Enabling stronger eutectic high-entropy alloys with larger ductility by 3D printed directional lamellae. *Addit Manuf.* **2021**;39:101901.
- [39] Nakashima K, Horita Z, Nemoto M, et al. Influence of channel angle on the development of ultrafine grains in equal-channel angular pressing. *Acta Mater.* **1998**;46(5):1589–1599.
- [40] Iwahashi Y, Horita Z, Nemoto M, et al. The process of grain refinement in equal-channel angular pressing. *Acta Mater.* **1998**;46(9):3317–3331.
- [41] Ding QQ, Fu XQ, Chen DK, et al. Real-time nanoscale observation of deformation mechanisms in CrCoNi-based medium- to high-entropy alloys at cryogenic temperatures. *Mater Today.* **2019**;25:21–27.
- [42] Ding QQ, Zhang Y, Chen X, et al. Tuning element distribution, structure and properties by composition in high-entropy alloys. *Nature.* **2019**;574:223–227.
- [43] Zhang ZJ, Sheng HW, Wang ZJ, et al. Dislocation mechanisms and 3D twin architectures generate exceptional strength-ductility-toughness combination in CrCoNi medium-entropy alloy. *Nat Commun.* **2017**;8:1–8.
- [44] Gludovatz B, Hohenwarter A, Thurston KVS, et al. Exceptional damage-tolerance of a medium-entropy alloy CrCoNi at cryogenic temperatures. *Nat Commun.* **2016**;7:1–8.
- [45] Gludovatz B, Hohenwarter A, Catoor D, et al. A fracture-resistant high-entropy alloy for cryogenic applications. *Science.* **2014**;345:1153–1158.
- [46] Zhang ZJ, Mao MM, Wang JW, et al. Nanoscale origins of the damage tolerance of the high-entropy alloy CrMnFeCoNi. *Nat Commun.* **2015**;6:1–6.
- [47] Laplanche G, Kostka A, Reinhart C, et al. Reasons for the superior mechanical properties of medium-entropy CrCoNi compared to high-entropy CrMnFeCoNi. *Acta Mater.* **2017**;28:292–303.
- [48] Yang MX, Pan Y, Yuan FP, et al. Back stress strengthening and strain hardening in gradient structure. *Mater Res Lett.* **2016**;4:145–151.
- [49] Zhu YT, Wu XL. Perspective on hetero-deformation induced (HDI) hardening and back stress. *Mater Res Lett.* **2019**;7:393–398.
- [50] Chen XF, Wang Q, Cheng ZY, et al. Direct observation of chemical short-range order in a medium-entropy alloy. *Nature.* **2021**;592:712–716.
- [51] Seol JB, Bae JW, Kim JG, et al. Short-range order strengthening in boron-doped high-entropy alloys for cryogenic applications. *Acta Mater.* **2020**;194:366–377.